

# Extended Red Objects and Stellar Wind Bow Shocks in the Carina Nebula

Remington O. Sexton<sup>1,2\*</sup>, Matthew S. Povich<sup>1</sup>, Nathan Smith<sup>3</sup>, Brian L. Babler<sup>4</sup>, Marilyn R. Meade<sup>4</sup>, & Alexander L. Rudolph<sup>1</sup>

<sup>1</sup>*Department of Physics & Astronomy, California State Polytechnic University, 3801 West Temple Avenue, Pomona, CA 91768, USA*

<sup>2</sup>*Department of Physics and Astronomy, University of California, Riverside, 900 University Avenue, Riverside, CA 92521, USA*

<sup>3</sup>*Steward Observatory, University of Arizona, 933 North Cherry Avenue, Tucson, AZ 85721, USA*

<sup>4</sup>*Department of Astronomy, University of Wisconsin, 475 North Charter Street, Madison, WI 53706, USA*

14 November 2021

## ABSTRACT

We report the results of infrared photometry on 39 extended red objects (EROs) in the Carina Nebula, observed with the *Spitzer Space Telescope*. Most EROs are identified by bright, extended 8.0  $\mu\text{m}$  emission, which ranges from 10'' to 40'' in size, but our sample also includes 4 EROs identified by extended 24  $\mu\text{m}$  emission. Of particular interest are nine EROs associated with late O or early B-type stars and characterized by arc-shaped morphology, suggesting dusty, stellar-wind bow shocks. These objects are preferentially oriented towards the central regions of the Carina Nebula, suggesting that these bow shocks are generally produced by the interactions of OB winds with the bulk expansion of the H II region rather than high proper motion. We identify preferred regions of mid-infrared color space occupied by our bow shock candidates, which also contain bow shock candidates in M17 and RCW 49 but are well-separated from polycyclic aromatic hydrocarbon emission or circumstellar discs. Color cuts identify an additional 12 marginally-resolved bow shock candidates, 10 of which are also associated with known late O or early B stars. H II region expansion velocities derived from bow shock candidate standoff distances are  $\sim 10 \text{ km s}^{-1}$ , assuming typical H II region gas densities, comparable to expansion velocities derived from bow shocks in M17 and RCW 49. One candidate bow shock provides direct evidence of physical interaction between the massive stellar winds originating in the Trumpler 15 and Trumpler 14 clusters, supporting the conclusion that both clusters are at similar heliocentric distances.

**Key words:** H II regions — infrared: ISM — open clusters and associations: individual (Carina Nebula) — shock waves — stars: early-type — stars: mass loss

## 1 INTRODUCTION

Massive stars are the cosmic engines that drive the turbulent evolution of their parent nebulae, creating observable feedback effects such as stellar-wind bow shocks. Wind velocities typical of massive late-O to early-B type stars can range between 900–3000  $\text{km s}^{-1}$  (Fullerton et al. 2006), exceeding the sound speed in their ambient medium (Castor et al. 1975) and forming ionized shock fronts. If the driving star itself has a supersonic velocity relative to the surrounding medium, ambient gas and dust can be swept around the star, forming a stellar-wind bow shock (van Buren et al. 1990). *Spitzer Space Telescope* observations of

the RCW 49 and M17 H II regions made as part of the Galactic Legacy Infrared Mid-Plane Survey Extraordinaire (GLIMPSE; Churchwell et al. 2009) revealed such stellar-wind bow shocks forming around late O to early B-type stars (Povich et al. 2008, hereafter P08), and similar dusty shock structures have been found in other massive star-forming regions (Kobulnicky et al. 2010; Gvaramadze et al. 2012). Smith et al. (2010, hereafter S10) identified 8 “extended red objects” (EROs) in *Spitzer* images of the South Pillars region of the Great Nebula in Carina, characterized by bright, extended emission in the 8.0  $\mu\text{m}$  bandpass of the Infrared Array Camera (IRAC; Fazio et al. 2004), and suggested that these objects are dusty bow shocks driven by late O and early B stars, similar to those found by P08.

\* Email: remington.sexton@email.ucr.edu

Located in the Sagittarius–Carina spiral arm at a dis-

tance of 2.3 kpc (Allen & Hillier 1993; Smith 2002, 2006a), the Carina Nebula is one of the few extreme massive star-forming regions close enough for detailed observation and unobscured by substantial reddening. It contains a large and varied population of high-mass stars, including 3 WNH stars, and over 70 O-type stars, some of which among the earliest ever discovered (Walborn et al. 2002). The central region of the Carina Nebula contains two massive clusters, Trumpler (Tr) 16 and Tr 14, which are the two largest contributors of stellar luminosity to the nebula (Smith 2006b). Tr 16 itself contains 43 known O-type stars, one of which is the luminous blue variable  $\eta$  Car (Smith 2006b). The combined ionizing luminosity, radiation pressure, and stellar winds from the other massive stars in Tr 16, Tr 14, and other sub-clusters throughout the Carina Nebula (S10; Feigelson et al. 2011) provide the feedback that drives the physical evolution of the nebula (Smith 2000).

The formation of bow shock structures around stars in and near H II regions gives insight into how massive star feedback shapes the local star-forming environment. Bow shock structures can be produced by the interaction between stellar winds from their driving stars and large-scale gas flows produced by the global expansion of H II regions and photoevaporation at the interfaces between H II regions and surrounding cold, molecular gas (P08, S10). Bow shocks also serve as a means for identifying candidate “runaway” OB stars escaping from their natal H II regions at high velocities (Gvaramadze & Bomans 2008; Kobulnicky et al. 2010; Gvaramadze et al. 2011).

Extending the work of S10, we identify 39 EROs from *Spitzer*/IRAC imaging of the full spatial extent of the Carina Nebula. The rest of this paper is organized as follows: In Section 2 we describe our ERO selection criteria, measurements of their geometries, and infrared (IR) photometry. In Section 3 we report results of these measurements, including the morphological classification of 9 EROs as candidate bow shocks and the classification of an additional 12 EROs as candidate bow shocks based on analysis of their mid-IR colors. In Section 4 we use measured (projected) standoff distances, empirical mass-loss rates and stellar wind velocities to estimate the velocity of the ambient interstellar medium (ISM) relative to the driving stars. We also discuss EROs that are not evident bow shock candidates, including two anomalous EROs, both of which exhibit resolved bow shock morphology, but fail on the criterion of color. Our conclusions are summarized in Section 5.

## 2 OBSERVATIONS AND DATA ANALYSIS

The *Spitzer* Vela-Carina survey<sup>1</sup> (S. R. Majewski, PI) observed the entire Carina Nebula using all four IRAC bandpasses, centred at 3.6, 4.5, 5.8, and 8.0  $\mu\text{m}$ , with a resolution of  $\sim 2''$  (Majewski et al. 2007; Povich et al. 2011b). Observations of the Carina Nebula with the Multiband Imaging Photometer for *Spitzer* (MIPS; Rieke et al. 2004) carried out during July 2007 as part of program GO-30848

<sup>1</sup> See [http://irsa.ipac.caltech.edu/data/SPITZER/GLIMPSE/doc/velacar\\_dataproduct\\_v1.0.pdf](http://irsa.ipac.caltech.edu/data/SPITZER/GLIMPSE/doc/velacar_dataproduct_v1.0.pdf)

<sup>2</sup> Available at [http://www.astro.wisc.edu/glimpse/glimpse\\_photometry\\_v1.0.pdf](http://www.astro.wisc.edu/glimpse/glimpse_photometry_v1.0.pdf)

(MIPSCAR; N. Smith, PI) provided 24.0  $\mu\text{m}$  imaging with approximately  $6''$  resolution (Povich et al. 2011b). The sensitivity of the IRAC and MIPS images to EROs was dramatically reduced in the central regions of the Carina nebula by the extreme mid-IR brightness of  $\eta$  Car and source confusion in the dense clusters Tr 14 and Tr 16.  $\eta$  Car itself was intentionally avoided by the MIPSCAR observation. The individual IRAC and MIPS frames were combined into large mosaics (1.2'' pixel scale) using the GLIMPSE data reduction pipeline (Benjamin et al. 2003; Churchwell et al. 2009).

“Residual images,” or mosaics with the point sources removed, are an advanced data product produced by the GLIMPSE pipeline and used in this study, as they facilitate photometry of extended sources such as EROs. The residual images (images with point sources removed) were produced by performing Point Spread Function fitting using a modified version<sup>2</sup> (Babler 2006) of DAOPHOT (Stetson 1987) on individual IRAC frames. The residual image tiles are mosaics from individual frame residuals. Thus if a source is extracted in some but not all frames it will show up in these images as a source. Sources may not be extracted for a variety of reasons, mainly due to cosmic ray contamination, saturation/non-linearity limits and along frame edges.

The data used by S10 consisted of a earlier and deeper set of IRAC observations limited to the South Pillars and south-western region of the nebula, avoiding the bright central regions surrounding Tr 16 and Tr 14 as well as the fields to the north. Utilizing the wider-field, Vela-Carina survey data allowed us to search the nebula in its entirety and enlarge our ERO candidate sample.

As part of an observing campaign targeting known and candidate OB stars in the Carina Nebula (NOAO Proposal #2013A-0181; M. S. Povich, PI), on 18 March 2013 we obtained spectra at 3975–4225  $\text{\AA}$  and 4250–4500  $\text{\AA}$  for 15 candidate ERO driving stars, including 4 lacking previous classifications, using the 2dF/AAOmega spectrograph on the Australian Astronomical Telescope (AAT). O stars and early B (B0-B2) stars were classified using the criteria and digital atlas of Walborn & Fitzpatrick (1990). Relative strengths of He II 4200 and He I+II 4026 were used most often to determine the spectral class for O stars. B stars were classified primarily using the strengths of He I lines (strongest at B2) the C III+O II blend near 4070, and Si IV 4089. Luminosity classes I and III were assigned primarily by the strength of Si IV 4089 and Balmer line absorption.

### 2.1 Identification of EROs

ERO candidates are characterized by extended 8.0  $\mu\text{m}$  emission, ranging from  $10''$  to  $40''$  in size (Table 1). The original S10 ERO selection criterion only identified EROs with some apparent arc-shaped morphology. We widened the original S10 selection criteria to include any visible extended emission at 8.0  $\mu\text{m}$  in close proximity to or shrouding a possible driving star, but apparently isolated from larger nebular structures. Our revised selection criteria, as well as the use of the wider-field Vela-Carina mosaics, allowed us to identify 32 additional candidate EROs beyond those originally found by S10, without bias for ERO emission, shape, or orientation, for a total sample of 39 EROs, including 7 from

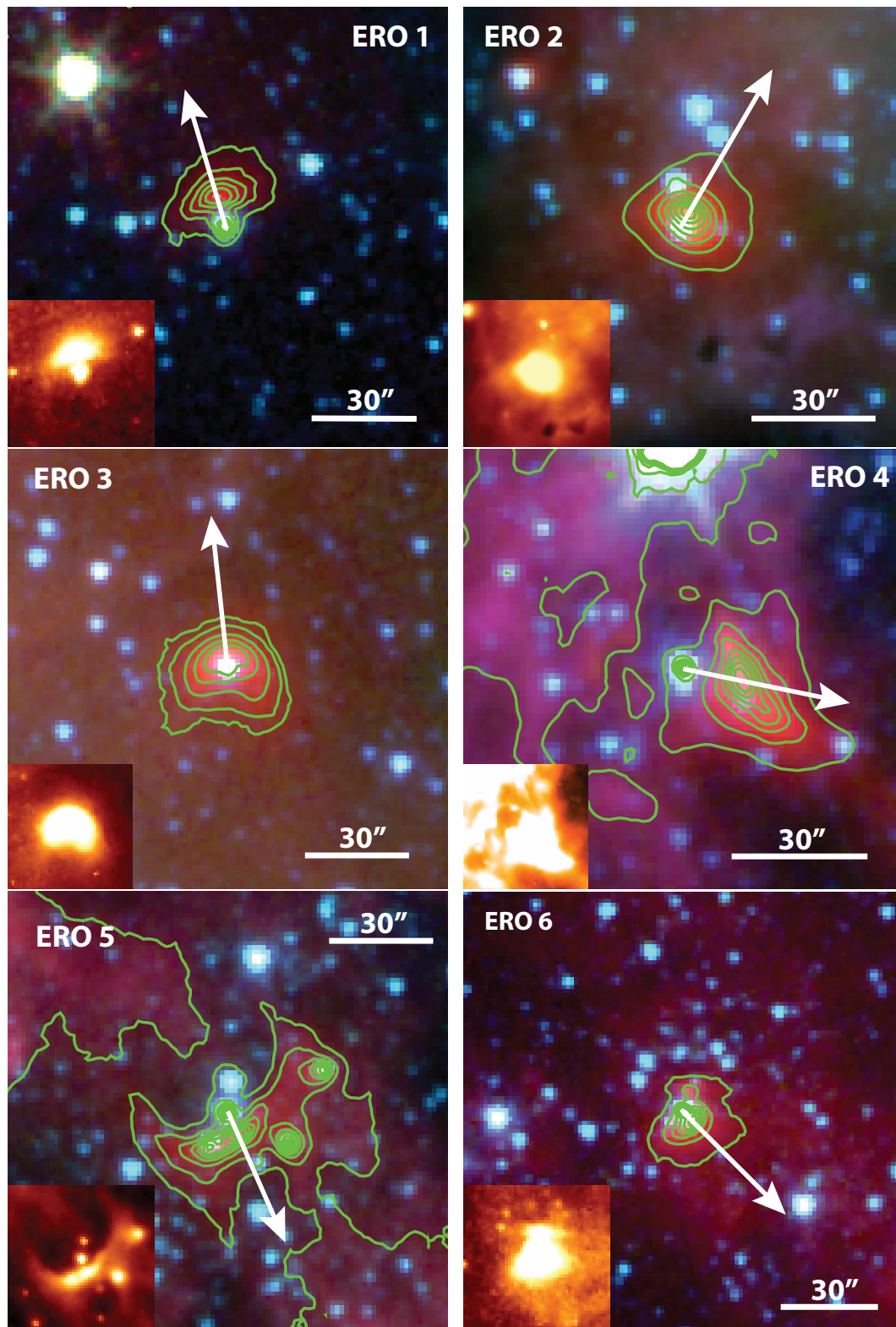


**Figure 1.** Composite 3-color images of bow shock candidates from ERO selection criterion (blue =  $3.6 \mu\text{m}$ , green =  $4.5 \mu\text{m}$ , red =  $8.0 \mu\text{m}$ ). An  $8.0 \mu\text{m}$  image of each ERO is inset at the bottom left of each image. Linearly-scaled  $8.0 \mu\text{m}$  contours are overlaid to outline the shape of each ERO. Arrows indicate the preferential orientation of each ERO.

S10 (ERO S1 from S10 was excluded from our sample, because it lacks an obvious driving star and is not sufficiently isolated from larger nebular structures). EROs 1–6 (Table 1 and Figure 1) exhibit clearly resolved bow shock morphologies, or asymmetrical arc shapes offset from the driving star, similar to those seen in P08.

Following Kobulnicky et al. (2010), we also identify any extended objects of interest in the 24.0  $\mu\text{m}$  MIPS images using analogous selection criteria to the 8.0  $\mu\text{m}$  EROs. Because much of the Carina Nebula itself produces very bright diffuse 24  $\mu\text{m}$  emission, our search was generally confined to the periphery of the nebula where background surface brightness was at a minimum. A total of four 24.0  $\mu\text{m}$  objects were found (EROs 36–39 in Table 1), three of which, EROs 36, 37, and 39, exhibit arc-shaped morphologies (Figure 2).

## 2.2 Size, Orientation, and Photometry

We used the longest angular dimension of extended emission (be it angular diameter for spheroidal objects or angular arc width for bow shock structures) as a proxy to measure the angular size of each ERO (Table 1). The location of the apparent driving star was determined using the 3.6  $\mu\text{m}$  images and the Vela-Carina point source catalog. Linearly scaled contours of the 8.0  $\mu\text{m}$  (or 24  $\mu\text{m}$ ) intensity provided a means to determining shape of the emission and locate the emission peak (Figure 1). Drawing a straight line from the location of the star to the point of highest 8.0  $\mu\text{m}$  (or 24  $\mu\text{m}$ ) intensity provided measurements of both the orientation angle and offset distance between the ERO and the driving star (Table 1). For bow shock candidates the offset distance gives the standoff distance between the shock front and the star projected onto the plane of the sky (see Figures 1 and 2).

Twenty-one EROs (including all 24  $\mu\text{m}$  objects) had measurable offset distances and orientations, including 11 with no clear bow shock morphology. These objects have both offset distances and orientations listed in Table 1. The contouring method also allowed us to measure orientations but not offset distances for EROs 13, 22, and 24. These three EROs are characterized by 8.0  $\mu\text{m}$  emission that is extended toward one side of the star but not the other, but the contour peak overlaps with the position of the star. For the remaining 15 EROs, the highest intensity of 8.0  $\mu\text{m}$  emission fell within the PSF of the star; these “spherically symmetric” EROs have no orientation listed in Table 1.

We performed photometry on all 39 ERO candidates using IRAF. To ensure that the photometry apertures we drew were consistent in each bandpass we convolved the IRAC images using a 2-D Gaussian with  $\sigma \approx 2.6$  pixels to match the 6'' resolution of the MIPS images. Median background subtraction was performed on PSF-subtracted images using the IRAF DAOPHOT FITSKY task (Stetson 1987), which also provided a standard deviation in counts for the background. Using the DAOPHOT POLYMARK task, we constructed by hand irregularly shaped apertures around each ERO using the convolved 8.0  $\mu\text{m}$  images (or the 24  $\mu\text{m}$  images for EROs 36–39). Background-subtracted flux densities were then measured (in MJy/sr) using the IRAF POLYPHOT task. We performed photometry on both the

mosaic and residual images produced by the GLIMPSE pipeline. Results from the mosaic photometry, which include the flux contributions from the driving stars, are reported in Table 3.

## 3 RESULTS

### 3.1 Morphological Bow Shock Candidates

P08 observed that bow shocks in both RCW 49 and M17 formed around late O stars. S10 similarly found that EROs in Carina tend to form around or near late O to early B-type stars. EROs 1–6 (Figure 1) and 24  $\mu\text{m}$  objects 36, 37 and 39 exhibit arc-shaped morphology in the contour analysis consistent with bow shocks (we refer to these as “morphological bow shock candidates” or MBSc). All MBSc are associated with known late O or early B-type driving stars (Table 1). EROs 1, 3, and 4 were previously identified by S10, but we do not classify the remaining 5 S10 EROs as MBSc.

Of the 9 MBSc, 6 show preferred “inward” orientations toward the centre of the Carina Nebula (Figure 3). EROs 1, 3, and 5 plus 24  $\mu\text{m}$  objects 37 and 39 are all generally oriented toward the central zone containing Tr 16 and Tr 14. ERO 2, located in projection between Tr 16 and Tr 14, is oriented toward Tr 14. EROs 4 and 6, plus 24  $\mu\text{m}$  object 36, have “transverse” orientation, and none of the MBSc have the “outward” orientation expected if the bow shocks were caused purely by the high space velocity of a runaway OB star escaping the Carina Nebula.

### 3.2 Additional Bow Shock Candidates from Color Analysis of EROs

Because many EROs are barely resolved, IR colors offer the potential for identifying additional bow shock candidates in the Carina Nebula and other, more distant H II regions. Emission features from polycyclic aromatic hydrocarbons (PAHs) tend to dominate broadband, IRAC images of H II regions (Peeters et al. 2004). Most diffuse objects in Carina have colors reflecting the strong PAH emission features at 3.3, 6.3, 7.7, and 8.6  $\mu\text{m}$ , which fall within the 3.6, 5.8, and 8.0  $\mu\text{m}$  IRAC filters, but there are no strong PAH features in the 4.5  $\mu\text{m}$  filter (Povich et al. 2007, S10).

We produced color-color diagrams of EROs to investigate whether EROs in general, and bow shock candidates in particular, exist in a color space distinguishable from unresolved, nebular PAH knots and other intrinsically red mid-IR point sources.

Figure 4 shows the colors of EROs with and without the contributions of their central stars to the IR flux. All photometry apertures were drawn to include the driving stars along with the extended emission itself. Not surprisingly, we find a general trend for EROs (with point sources) to move redward in both [4.5]–[5.8] and [5.8]–[8.0] when their point sources are subtracted. Uncertainties on colors significantly increase when point sources are removed, mostly due to low signal-to-noise at 4.5  $\mu\text{m}$ , as emission in this bandpass is dominated by the candidate driving stars rather than the EROs. For the remaining analysis, we employ ERO photometry including the contributions of the associated driv-

**Table 1.** ERO positions, geometric properties, and probable driving stars. EROs 1-35 are objects identified using the 8.0  $\mu\text{m}$  IRAC images; EROs 1-6 are additionally morphological bow shock candidates. EROs 36-39 were identified using the 24.0  $\mu\text{m}$  MIPS images. EROs 1, 3, 4, 18, 24, 25, and 31 were previously identified by S10. Coordinates refer to the positions of the candidate ERO driving stars. Unless indicated otherwise, published spectral types are from Gagné et al. (2011). New AAT spectral types are from our 2dF/AAOmega spectroscopic observations.

ERO	$\alpha_{2000}$	$\delta_{2000}$	Size (asec)	Offset (asec)	Orientation (deg W of N)	Star	Spectral Type	
							Published	AAT
EROs showing resolved bow shock morphology								
1	10:43:17.907	-60:08:03.460	16.7	8.6	-13	HD 93027	O9.5 IV	O9.5 V
2	10:44:00.904	-59:35:46.040	15.3	4.7	34	Tr 14-127	O9 V	O9 V
3	10:44:11.116	-60:03:21.283	20.9	3.0	-6	HD 305536	O9.5 V	
4	10:44:36.204	-60:05:29.074	32.9	12.1	101	HD 93222	O7 V	O8 V
5	10:44:43.860	-59:21:25.414	11.3	6.0	152	HD 93249 <sup>a</sup>	O9 III	
6	10:49:24.933	-59:49:44.125	13.7	3.4	132	HD 305599	B0 Ib	
Other EROs								
7	10:38:34.415	-59:43:10.861	11.6					
8	10:40:19.370	-59:49:09.479	13.8					
9	10:40:29.175	-58:53:23.162	7.6	7.2	144			
10	10:40:49.119	-59:50:27.150	11.2					
11	10:40:50.810	-58:52:27.934	11.6					
12	10:41:06.765	-58:50:06.036	7.0					
13	10:42:45.146	-59:52:19.672	12.1		-12	HD 305437	B0.5 V	B0 V
14	10:43:09.463	-59:24:53.87	11.8				YSO <sup>b</sup>	
15	10:43:11.145	-59:44:21.266	10.7	14.4	22	HD 303316	O6 V	O6 V
16	10:43:12.181	-59:00:54.204	7.4					
17	10:43:15.697	-59:51:05.066	11.0			HD 305516	B0.5 V	
18	10:43:20.289	-60:13:01.348	59.3	15.5	-91	TYC 8957-99-1		B8
19	10:43:43.771	-58:42:20.749	16.8	1.6	36			
20	10:43:43.959	-59:48:18.132	12.8	15.4	-102	HD 305518	O9.5 V	O9/O9.5 V
21	10:44:05.107	-59:33:41.469	20.2	7.6	44	Tr14-29	B1.5 V <sup>c</sup>	B2 V
22	10:44:05.786	-59:35:10.755	6.8		67	Tr 14-124	B1V	
23	10:44:30.184	-59:26:12.723	7.4	6.9	144	TYC 8626-2506-1	O9 V(n) <sup>d</sup>	O9.5 V <sup>b</sup>
24	10:44:50.402	-59:55:45.188	15.2		-5	CPD-59 2605	B1 V	
25	10:45:13.359	-59:57:54.092	15.3			HD 305533	B0.5 Vnn	B1 V
26	10:45:20.420	-59:17:06.526	14.7			HD 303300		O9.5 V <sup>b</sup>
27	10:45:38.315	-60:36:15.023	10.8					
28	10:45:46.936	-59:54:57.484	9.9				YSO <sup>b</sup>	
29	10:46:11.525	-58:39:11.410	16.8	5.2	14	CPD-57 3781	O8 V <sup>e</sup>	
30	10:46:13.585	-59:58:31.381	10.7					
31	10:46:53.817	-60:04:42.114	19.8	4.7	68	HD 93576	O9 IV	O9 V
32	10:47:45.428	-60:25:56.791	15.1	1.7	-122			
33	10:47:48.007	-59:41:30.955	11.2	11.3	52			
34	10:48:24.302	-60:08:00.830	12.3				YSO <sup>b</sup>	
35	10:51:11.555	-59:48:44.916	18.2					
Extended 24 $\mu\text{m}$ objects								
36	10:40:12.382	-59:48:10.326	106.2	15.7	-118	HD 92607	O8 V	O8.5 V+O9 V <sup>f</sup>
37	10:47:38.891	-60:37:04.451	174.6	17.1	41	HD 93683	B0.5 Vne <sup>g</sup>	O9 V
38	10:47:46.173	-60:24:36.173	25.4	7.3	25		OB <sup>b,h</sup>	
39	10:48:46.555	-60:35:40.461	27.6	5.8	16	CPD-59 2735		B0 V

<sup>a</sup> HD 93249, or CD-58 3536, is the most luminous star in the Tr 15 cluster. It has a visual companion, CD-58 3536B O9.5 III (see, e.g., Wang et al. 2011, and references therein) whose wind likely also contributes to driving ERO 5.

<sup>b</sup> Candidate OB or YSO from Povich et al. (2011a,b).

<sup>c</sup> Identification and spectral type from Ascenso et al. (2007). The driving star is identified as Trumpler 14 MJ 218 by Ngoumou et al. (2013).

<sup>d</sup> New Galactic O Star Catalog spectral type from (Sota et al. 2014).

<sup>e</sup> Spectral type from Reed (2003)

<sup>f</sup> Double-lined spectroscopic binary.

<sup>g</sup> Be spectral type reported by Houk & Cowley (1975).

<sup>h</sup> Preliminary near-IR spectroscopy with the Southern Astrophysical Research (SOAR) telescope indicates an early-type star (M. Alexander, private communication, 2014).

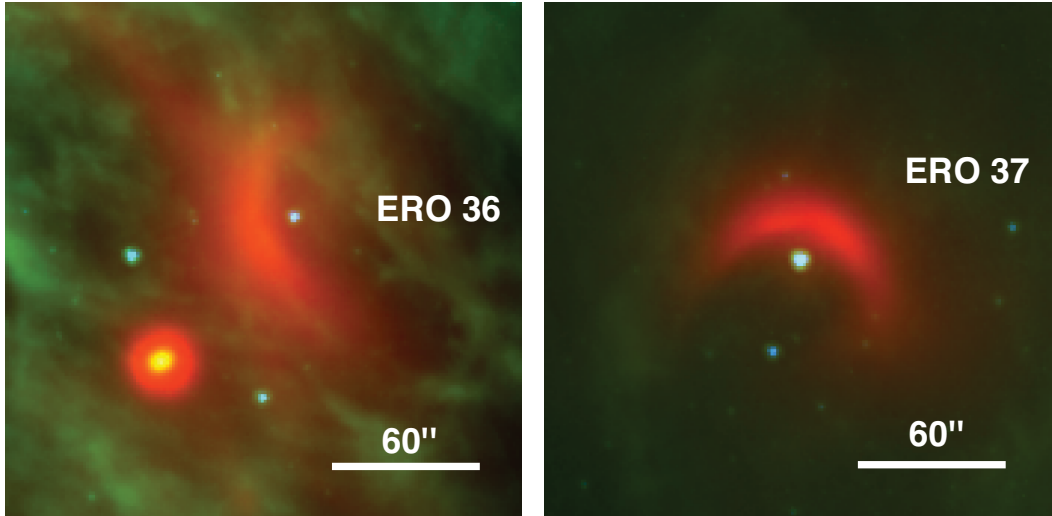


**Figure 2.** Composite 3-color images of the two  $24.0 \mu\text{m}$  bow shock candidates with the clearest arc morphologies (blue =  $4.5 \mu\text{m}$ , green =  $8.0 \mu\text{m}$ , red =  $24.0 \mu\text{m}$ ).

ing stars (Table 3) because the stellar contribution will be inevitably included for unresolved EROs.

We next compared the colors of EROs (with their central stars included; Table 3) to a subset of intrinsically red IR point sources from the MYStIX IR Excess Source catalog (MIREs; Povich et al. 2013). We defined our comparison sample as those MIREs objects found in IRAC data processed through the GLIMPSE pipeline and associated with massive star-forming regions similar to the Carina Nebula, with distances ranging from 2–4 kpc. Using the classifications of the MIREs catalog, we separate sources into three primary regions on the  $[4.5] - [5.8]$  vs.  $[5.8] - [8.0]$  color plane (Figure 5): (1) nebular PAH knots, (2) young stellar objects (YSOs) with dusty, circumstellar discs/envelopes, and (3) PAH-dominated emission from unresolved, external starbursting galaxies. We find that 14 of the 39 EROs fall within the PAH quadrant, while only 3 fall within the color space designated for YSOs. The remaining EROs reside within the color space designated for starburst galaxies, however EROs are unlikely to be confused with background galaxies because (1) these EROs are even redder in  $[5.8] - [8.0]$  and (2) EROs associated with Galactic OB stars should be much brighter in the mid-IR compared to unresolved, external galaxies.

EROs falling outside the PAH or YSO quadrants tend to occupy a distinct, box-shaped region (dashed line in Figure 5) defined by

$$1.5 \leq [5.8] - [8.0] \leq 3.1 \text{ (mag)},$$

$$0 \leq [4.5] - [5.8] \leq 1.8 \text{ (mag)}.$$

This “ERO box” contains all of the  $8 \mu\text{m}$  MBSs from both this paper and P08 (12 total), plus two of the three  $24 \mu\text{m}$  MBSs (ERO 37 is the outlier). It also contains 12 other EROs that we hereafter designate “color bow shock candidates,” or CBSs: EROs 8, 17, 20, 22, 23, 24, 25, 26, 28, 29, 31, and 33. Ten of these are associated with known OB stars (Table 1), including the remaining 5 EROs from S10. Of the 7 CBSs with measurable orientations, 5 are oriented inward, similar to the MBSs.

In Figure 6 we compare the  $[5.8] - [8.0]$  vs.  $[8.0] - [24]$  colors of EROs (again including contributions from the driving stars) to objects in the Pan-Carina YSO Catalog (PCYC; Povich et al. 2011b), which, unlike the MIREs catalog, includes  $24.0 \mu\text{m}$  point-source photometry. This color plane divides into 3 principal regions. Bow shock candidates are again separated from most YSOs by the line at  $[5.8] - [8.0] = 1.5$  mag defining one side of the “bow shock box” from Figure 5. EROs falling within the PAH region of Figure 5 are much bluer than bow shock candidates in  $[8.0] - [24]$ ; providing another (loose) constraint on CBS colors:

$$[8.0] - [24] > 2 \text{ (mag)}.$$

All CBSs and MBSs are found in the range  $2.7 < [8.0] - [24] < 5$  mag, similar to disc-dominated YSOs in the PCYC. The PCYC also includes a population of much redder sources (to  $[8.0] - [24] \sim 8$  mag) corresponding to embedded protostars (Povich et al. 2011b).

Four EROs fall within the YSO color region in both Figures 5 and 6. ERO 37 is the  $24 \mu\text{m}$  MBS with anomalous colors, perhaps the one true “ $24 \mu\text{m}$ -only” bow shock in our sample. ERO 38 is the one  $24 \mu\text{m}$  source with ambiguous morphology; it may be a bow shock or part of a larger IR bubble structure around a candidate OB star (Povich et al. 2011a). ERO 13 is associated with a B0.5 star, and while its colors are consistent with a circumstellar disc, its projected location in the middle of the Carina Nebula’s southern evacuated superbubble lobe (Figure 3) seems to argue against extreme youth, while its directly inward orientation favors a bow shock interpretation. ERO 15 is associated with an O6 star, an early type compared to other bow shock candidates; it may instead be the brightest part of an IR bubble structure excited by that star.

Three EROs are the resolved  $8 \mu\text{m}$  counterparts to PCYC point sources. EROs 14 and 28 are associated with the point sources PCYC 179 and 990, respectively (Figure 6); both EROs are redder in  $[5.8] - [8.0]$  but much bluer (by  $\sim 2$  mag) in  $[8.0] - [24]$  compared to the point sources.

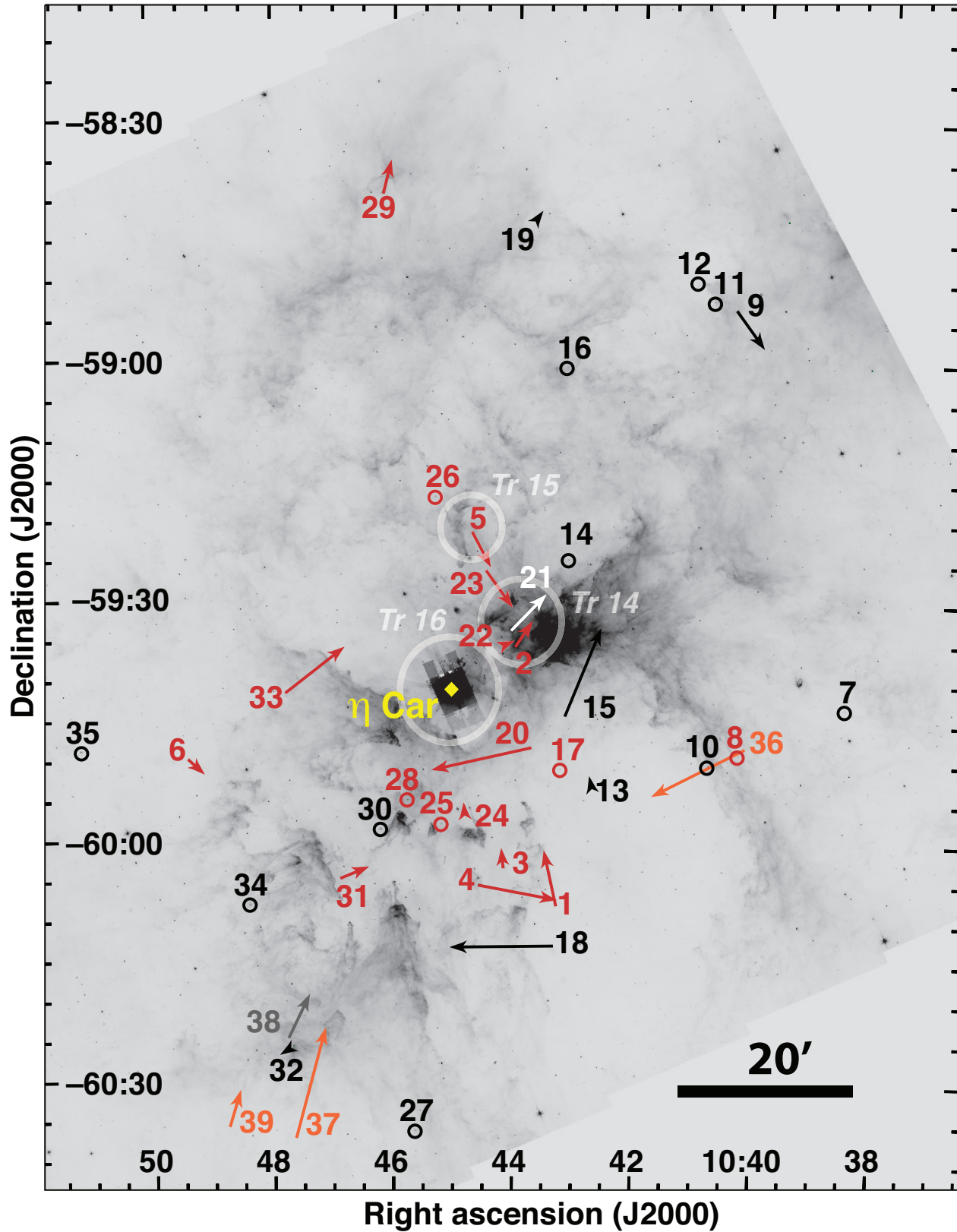


**Figure 3.** Grayscale 8  $\mu\text{m}$  image of the region of Carina Nebula searched for EROs. Morphological, 8  $\mu\text{m}$  bow shock candidates (EROs 1-6) are labelled as red arrows, other EROs (7-35) are black or white, 24.0  $\mu\text{m}$  bow shocks (36, 37, and 39) are orange, while the other 24  $\mu\text{m}$  objects (38) is gray. Lengths of the arrows correspond to approximate standoff distances scaled up by a factor of 50, and directions represent ERO orientations measured using intensity contours (Table 1). Circles mark EROs without measurable orientations. Locations of the principal ionizing clusters of the Carina Nebula, Tr 14, 15, and 16 are circled.

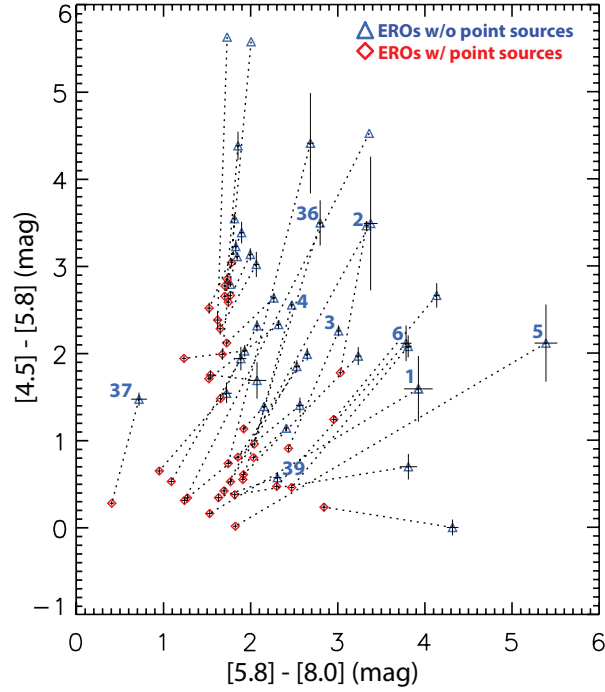


**Figure 4.**  $[4.5]-[5.8]$  versus  $[5.8]-[8.0]$  color-color diagram of EROs in Carina. Each ERO is plotted twice, once with emission from the associated point source included in the color (diamonds) and once without point source emission (triangles) connected by dashed line segments. Morphological bow shock candidates are labelled by their ERO number.

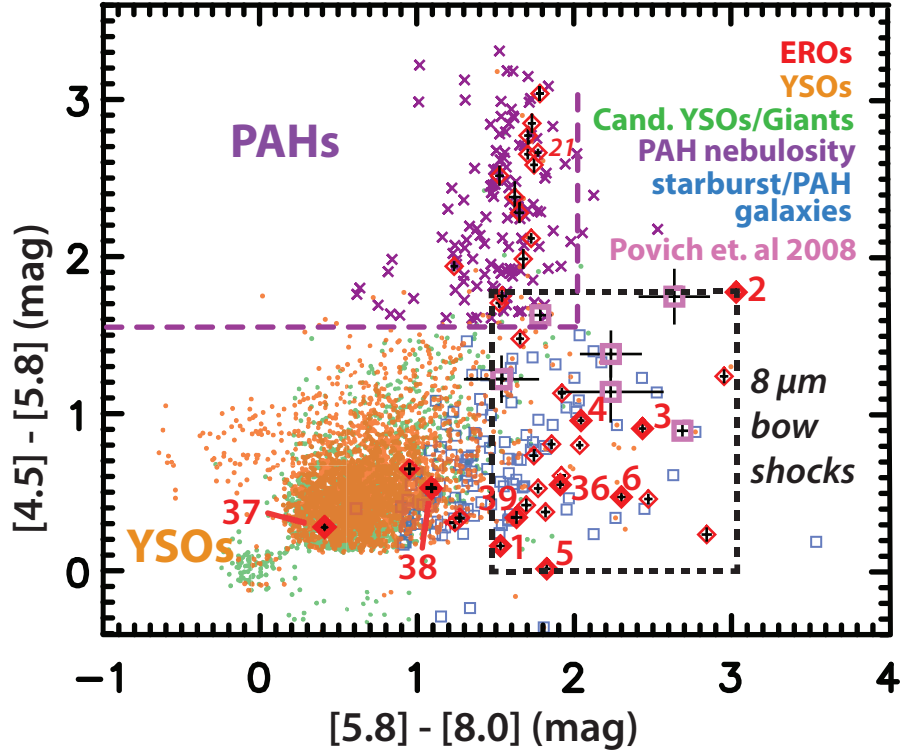


**Figure 5.**  $[4.5]-[5.8]$  versus  $[5.8]-[8.0]$  color-color diagram of EROs presented in this paper, M17 and RCW49 bow shocks from P08, and various classes of intrinsically red IR point sources classified in the MIREs catalog (Povich et al. 2013). Morphological and  $24\ \mu\text{m}$  bow shock candidates are labelled by their ERO number (Table 1). Morphological  $8\ \mu\text{m}$  bow shocks are found within the region of color space bounded by the short-dashed black box. Colors are based on the photometry in Table 3 and include flux from the associated driving stars.

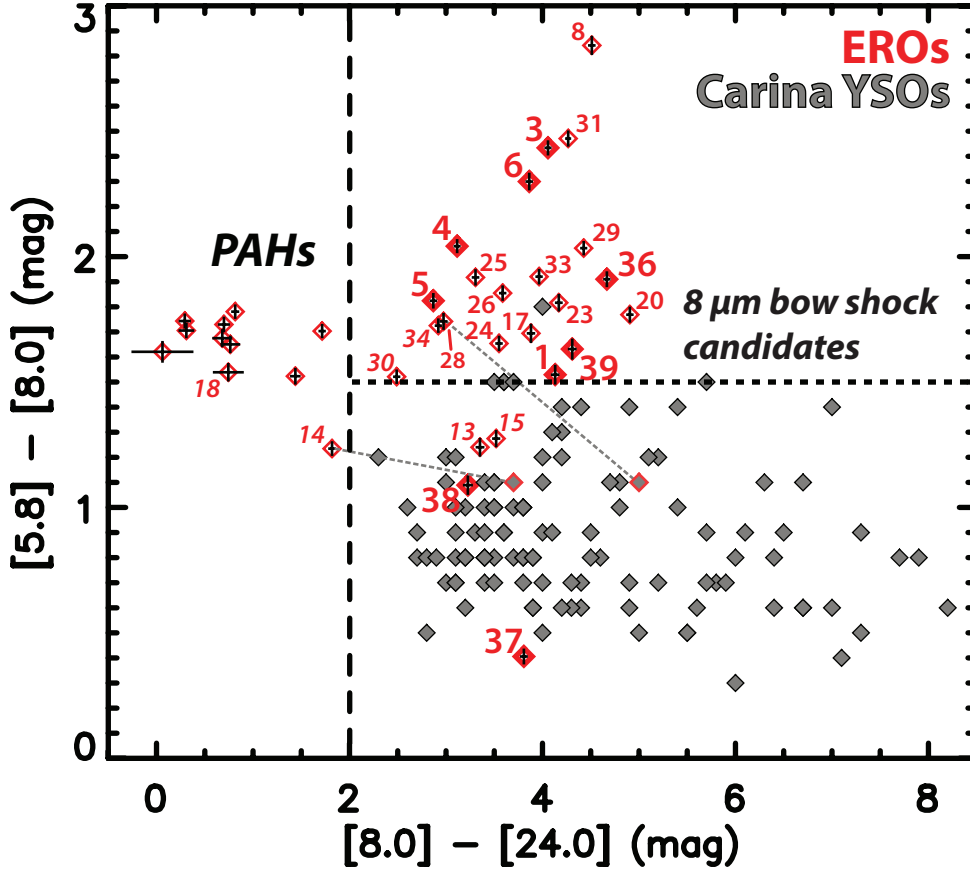


**Figure 6.**  $[5.8] - [8.0]$  versus  $[8.0] - [24.0]$  color-color diagram comparing EROs to Carina YSOs from the PCYC (Povich et al. 2011b). Dashed lines separate regions of this color space containing YSOs, bow shock candidates, and PAH nebular knots. MBSs are labelled with bold numbers, CBSs are labelled with smaller numbers, and other notable EROs are labelled with italicized numbers. EROs 14 and 28 are associated with the point sources PCYC 179 and 990, respectively (joined by dashed gray lines).

This suggests that our aperture photometry extracted preferentially more  $8 \mu\text{m}$  flux compared to the PCYC point-source photometry (which used the GLIMPSE pipeline for the IRAC filters and a custom  $24 \mu\text{m}$  aperture photometry procedure; Povich et al. 2011b). Neither ERO 14 nor 28 has a discernible orientation (Figure 3); they are consistent with YSOs with large, marginally resolved circumstellar discs. ERO 34 corresponds to PCYC 1367, a *Midcourse Space Experiment* point source (but not an IRAC point source, hence not among the PCYC sources plotted in Figure 6). It is not associated with a known OB star, but it may be a massive YSO (Povich et al. 2011b).

## 4 DISCUSSION

### 4.1 Bow Shocks as ISM “Weather Vanes”

Bow shock candidates (MBSs and CBSs) associated with OB stars are of particular interest as probes of massive star feedback processes and the relative motions between massive stars and the ISM in H II regions. EROs 1, 3, 24, 31, 37 and 39, all located in the South Pillars region, are generally aligned with the various pillars (S10) and oriented in the inward direction toward Tr 14 & 16 (Figure 3). This preferred orientation suggests that these bow shocks are caused

by the interaction of the driving OB stellar wind with the global feedback processes (thermal gas pressure, radiation pressure, and/or cluster winds) powering the expansion of the H II region and eroding the pillars. EROs 2, 22, and 23 are all in closer proximity to Tr 14 than to Tr 16, and are all oriented toward the centre of the Tr 14 cluster, indicating that they are reacting to feedback from Tr 14 only. No EROs appear oriented toward Tr 16 but not Tr 14; this may be due to the fact that Tr 14 is a very dense, centrally concentrated cluster while Tr 16 is a looser aggregate of multiple subclusters (Feigelson et al. 2011).

ERO 5 is a particularly interesting case. It is apparently driven by the visual binary stars HD 93249 (or CD-58 3536A) and CD-58 3536B, the most luminous members of the Tr 15 cluster (Wang et al. 2011). ERO 5 is oriented directly toward the centre of the Tr 14 cluster, however, providing direct evidence that feedback from Tr 14 completely overwhelms that of the significantly older, less massive and less luminous Tr 15. This evidence of physical interaction between the clusters provides further support that both clusters are at the same heliocentric distance and hence part of the Carina Nebula Complex.

Five bow shock candidates associated with OB stars, EROs 4, 6, 20, 29, and 36, are not oriented toward the centre of the Carina Nebula. These divergent orientations have two possible causes: (1) locally non-radial components to the

ambient ISM flow, perhaps produced by photoevaporative flows off of nearby molecular clouds (S10), or (2) high space velocity of the driving star, as with the candidate “run-away” OB stars identified via IR bow shocks found near other massive Galactic star-forming regions (Gvaramadze & Bomans 2008; Kobulnicky et al. 2010; Gvaramadze et al. 2011). ERO 4 is perhaps the best candidate for a bow shock interacting with a photoevaporative flow, as it is oriented toward the inner side of the large pillar demarcating the western boundary of the South Pillars region. ERO 29 is a candidate runaway O8 V star, as it is located on the northern periphery of the Carina Nebula and is oriented almost precisely outward from the centre (Figure 3). To confirm the runaway star scenario requires a better understanding of the complex kinematics of the Carina stellar population. Interpreting velocity measurements for individual OB stars begins with defining a reliable reference frame, correcting for Galactic rotation and streaming motions, as well as accounting for cluster dynamics. Additional radial velocity and proper motion data should give further insight to the potential runaway status of the Carina bow shock driving stars in the future.

#### 4.2 Physical Conditions Governing Emission Processes and Colors of IR Bow Shocks

Our analysis of the IR colors of EROs (Section 3.2) supports the conclusions of P08, S10, and Kobulnicky et al. (2010) that IR emission from bow shocks associated with OB stars in H II regions originates from dust entrained within the (pre-shock) plasma and heated by the nearby OB star (P08). Because O and B-type stars are not efficient dust producers, we echo S10 in proposing that the source of dust is (photo)evaporating molecular clouds, such as the molecular cloud formations being ablated in the South Pillars region. Everett & Churchwell (2010) calculated that dust on the order of  $a \leq 0.1 \mu\text{m}$  will typically be evacuated from a wind-blown H II region cavity on time-scales of  $10^4$  years, and any dust grains on the order of  $a \simeq 0.001 \mu\text{m}$  will be destroyed, hence dust must be continually replenished and likely does not survive passage through the stellar-wind bow shocks. The wind momenta of massive stars places additional constraints on the types of stars that can drive IR bow shocks, because the winds cannot be so strong such that they completely clear away the surrounding dust and gas (P08, S10). This interpretation favors IR bow shocks forming around late O and early B stars on the periphery of young, dusty, star-forming regions, fitting the general picture of the Carina Nebula (Figure 3).

We have demonstrated that dusty bow shocks associated with early-type stars generally occupy regions of IR color space that are distinct from the colors of the most likely contaminating sources, PAH nebular knots and YSOs. PAH knots are redder in [4.5] – [8.0] but bluer in [8.0] – [24] compared to CBSc. This is explained by the presence of strong PAH emission features falling within the [5.8] and [8.0] bandpasses but not in the [4.5] or [24] bandpasses. Evidently IR bow shocks associated with OB stars do not excite strong PAH emission, and this explains why EROs are visually distinguishable from the ambient PAH nebulosity in our multiband *Spitzer* color images (Figure 1). There

are several possible physical reasons for this dearth of PAH emission: (1) the dust entrained within the bow shocks was PAH-depleted already, typical for dust within H II regions (Povich et al. 2007; Everett & Churchwell 2010), (2) PAH molecules mixed within the pre-shock gas and dust are destroyed by FUV radiation from the OB driving star, or (3) PAH molecules are destroyed by the passage through the shock front itself.

CBSc are redder than YSOs in [5.8] – [8.0] (Figure 5), but the [8.0] – [24] colors of CBSc are similar to disc-dominated YSOs, and protostars extend to much redder [8.0] – [24] colors (Figure 6). This indicates that the emitting dust in bow shocks is generally warmer than the dust in protoplanetary discs and protostellar envelopes. Another difference is that YSOs, especially protostars, often exhibit deep silicate absorption at  $9.7 \mu\text{m}$ , which suppresses flux in the [8.0] band. This absorption is not expected to be present in IR bow shocks, which should be optically thin (P08) and possibly exhibit the silicate feature in *emission*.

#### 4.3 Probing ISM Pressure and Velocity in the Carina Nebula

Following P08, we quantify the physical parameters governing the observed bow shock morphology to measure the momentum flux of the ambient ISM at different locations within the Carina Nebula. We calculate the ambient momentum flux of the ambient ISM at the standoff distance  $d_w$  of the bow shock, that is, the point at which momentum flux is balanced by the driving star’s stellar wind, as

$$n_w v_w^2 = n_0 v_0^2,$$

where  $v_0$  is the *relative* velocity between the driving star and the ambient ISM. We normalize the values for mean ISM particle density, stellar mass-loss rates, and terminal wind velocities such that  $n_{0,3} = n_0 / (10^3 \text{ cm}^{-3})$ ,  $\dot{M}_{w,-6} = \dot{M}_w / (10^{-6} M_\odot \text{ yr}^{-1})$ , and  $v_{w,8} = v_w / (10^8 \text{ cm s}^{-1})$ , following van Buren et al. (1990), P08, and Kobulnicky et al. (2010). Assuming that mass-loss about the star is spherically symmetric, it can be written as

$$\dot{M}_w = 4\pi d_w^2 \mu n_w v_w,$$

where  $\mu = 2.36 \times 10^{-24} \text{ g}$  is the mean ISM gas mass per hydrogen atom. Solving for  $v_0$ , we have

$$v_0 = 1.5 \left( \frac{d_w}{\text{pc}} \right)^{-1} \left( \dot{M}_{w,-6} v_{w,8} \right)^{1/2} n_{0,3}^{-1/2} \text{ [km s}^{-1}]. \quad (1)$$

The resulting values for  $v_0 n_{0,3}^{1/2}$  derived from each of the MBSc, are presented in Table 2. These are comparable to values cited by P08, indicating that overall the MBSc in the Carina Nebula probe similar ISM conditions as found in M17 and RCW 49. As found by Fullerton et al. (2006), and noted in P08, mass-loss rates have a high dependence on spectral type and are therefore the largest source of uncertainty in our calculations. Indeed, citing the high uncertainty in mass-loss rates, Kobulnicky et al. (2010) turned the problem around, assuming reasonable values for the ambient density and relative velocities of OB stars to the ISM to use bow shocks as constraints on the stellar wind momentum and hence mass-loss rates.

Equation 1 must be interpreted with caution. Order-of-magnitude uncertainties in mass-loss rates (Kobulnicky

et al. 2010) create factors of  $\sim 2$  uncertainty in  $v_0$ . All results are modulo an unknown inclination angle with respect to the plane of the sky (although  $\cos i$  is likely to be near unity for MBSc, otherwise the arc shape would not be visually apparent, see P08). The density of ionized plasma in the Carina Nebula likely varies by factors of several about the typical value of  $n_{0,3} = 1$  (Brooks et al. 2003), but this effect is subordinate to the uncertainties in the mass-loss rates. More importantly, the derived values for  $v_0$  (assuming  $n_{0,3} = 1$ ) are comparable to the  $\sim 10 \text{ km}^{-1}$  sound speed in the ionized plasma. In the case where the relative velocity between the star and the ambient ISM is not highly supersonic, thermal (and possibly turbulent) pressure in the ambient medium become important relative to ram pressure in balancing the stellar wind pressure. Accounting for thermal pressure adds a term, proportional to the square of the sound speed, to our momentum flux balance equation, which becomes

$$n_w v_w^2 = n_0 v_0^2 + 2 \frac{n_0}{\mu} k_B T_0$$

(note that the wind itself is highly supersonic, hence the thermal pressure term on the left-hand side can still be safely neglected). Normalizing the ambient temperature to  $T_{0,4} = T_0 / (10^4 \text{ K})$ , we derive a correction to the relative velocity from Equation 1,

$$v'_0 = (v_0^2 - 117 T_{0,4})^{1/2}. \quad (2)$$

This correction is independent of the ambient density, and for H II regions  $T_{0,4}$  is near unity. We can thus apply Equation 2 to correct our values of  $v_0 n_{0,3}$  for the expected contribution of thermal pressure, except for two cases (EROs 1 and 37) where the thermal pressure term exceeds the ram pressure term ( $v_0 < \sqrt{117} \text{ km s}^{-1}$ ). Corrected values of  $v'_0 n_{0,3}$  are included in Table 2; in the majority of cases these corrections are small compared to the uncertainties in  $v_0$ .

S10 used the observed bow shock standoff distances to constrain the *total* pressure in the ambient medium balanced by the stellar wind pressure,

$$p_0 = \frac{1}{13} \left( \frac{d_w}{\text{pc}} \right)^{-2} \dot{M}_{w,-6} v_{w,8} \quad [10^{-9} \text{ dyne cm}^{-2}]. \quad (3)$$

This approach does not assume any particular geometry for the shock front, does not require a distinction of ram pressure from other sources of ambient pressure, and does not depend on the density or temperature of the ambient gas. Equation 3 is, however, more sensitive to uncertainties in mass-loss rates and standoff distances than Equation 1. We list values for  $p_{0,-9} = p_0 / (10^{-9} \text{ dyne cm}^{-2})$  in Table 2, these are consistent with the values of  $p_{0,-9} = 1.8, 4.8,$  and  $8.6$  derived for EROs 1, 3 and 4, respectively, by S10, the differences reflecting the adoption of different mass-loss rates for the driving stars.

#### 4.4 Anomalous, Arc-Shaped EROs

Two notable EROs have arc-shaped morphology but are not counted among our MBSc.

ERO 21, identified by Ascenso et al. (2007) as a compact nebula with bow shock morphology in VLT *JHK<sub>s</sub>* images (and included in the S10 list of EROs as S9, although it fell outside the boundary of the IRAC images analysed

in that work), also appears arc-shaped in the Vela–Carina IRAC images (Figure 7). Contour analysis of ERO 21 confirms that peak emission at  $8.0 \mu\text{m}$  occurs between the direct line of sight between its driving star and the centre of Tr 14. The  $[4.5] - [5.8]$  and  $[5.8] - [8.0]$  colors of ERO 21 place it deep within the region dominated by PAH nebulosity (Figure 5), and these anomalous colors prevent us from classifying this object as an MBSc. The original Ascenso et al. (2007) classification of ERO 21 as a “compact nebula” rather than a dusty bow shock appears appropriate, as its mid-IR colors indicate that this object is likely the tip of an elongated column of high-density gas and dust, similar to the numerous star-forming pillars observed elsewhere in the Carina Nebula. ERO 21 is, however, driven by an early B1.5 V star, which are known to have strong winds associated with stellar wind bow shocks, so it is certainly possible that an irradiated shock front has formed at the tip of the pillar. We measured a standoff distance of  $0.084 \text{ pc}$ , similar to the  $8.0 \mu\text{m}$  MBSc listed in Table 2, giving ambient ISM properties around ERO 21 of  $v_0 n_{0,3}^{1/2} \approx 4$  and  $p_{0,-9} = 2.2$ , both on the low range compared to other EROs, especially the nearby (in projection) ERO 2 (Figure 3).

Ngoumou et al. (2013) named ERO 21 “the sickle” and proposed a model in which the wind of a runaway B star interacts with an ambient density gradient in a low-density envelope surrounding a nearby, compact clump of molecular material. The bow-shock hence forms as a consequence of the high velocity of the driving star, Trumpler 14 MJ 218, which has a UCAC proper motion of  $95 \text{ km s}^{-1}$  at position angle  $37^\circ$  (W of N). If this interpretation is correct, the unusual, PAH-dominated colors of ERO 21 might be explained by the proximity of MJ 218 to a molecular clump of a nearby pillar, which is externally illuminated by either the B star itself or the nearby O stars in Tr 14. Unlike our other bow shock candidates, the globule must be sufficiently dense either to shield PAH molecules from destruction or to provide a sufficient supply of PAH-rich gas and dust to replenish IR-emitting arc. While the uncertainties are quite large  $\sim 50\%$ , the proper motion is consistent with the orientation of ERO 21 (Table 1), which is the strongest evidence favoring the runaway star bow shock interpretation.

The runaway star interpretation, however, has some important caveats. Ngoumou et al. (2013) note that the proper motion of MJ 218 is consistent with a runaway B star from Tr 16. They also note that the star is detected in X-rays (Broos et al. 2011), and explain (reasonably) that the X-rays are produced by a low-mass, binary companion to the B star. It is not clear that such a binary system could survive a dynamical interaction (such as an N-body encounter or supernova explosion of the most massive star in an originally triple or higher-multiplet system) capable of ejecting it at  $\sim 100 \text{ km s}^{-1}$  from Tr 16. It is possible that the proper motion measurements are unreliable, given that the large distance to Carina, crowded field, and high background nebulosity conspire to make automated proper motion measurements very difficult. The choice of a reliable zero-velocity reference frame is again very important. The implicit assumption that the Carina Nebula as a whole has zero proper motion may apply thanks to its proximity to a Galactic rotation tangent point, but it is far from clear that the assumption of zero proper motion for Tr 16 and other individual (sub)clusters is valid. The *Chandra* Carina

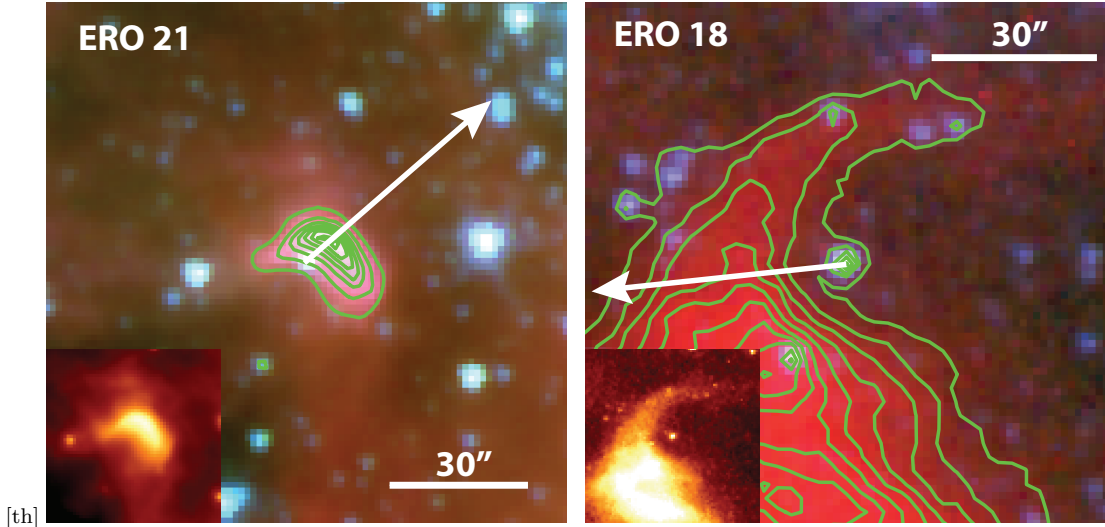


**Figure 7.** Composite 3-color images of ERO 21 (compact nebula from Ascenso et al. 2007) and ERO 18 with the same color-coding, inset images, contours, and overlays as in Figure 1.

**Table 2.** Bow shock standoff distances and estimated stellar wind properties. Estimates of stellar mass-loss rates and wind-velocities are based on Vink et al. (2001), Brooks et al. (2003), Fullerton et al. (2006), Smith (2006b), Muijres et al. (2012a), and Muijres et al. (2012b).

ERO	Spectral Type	$\dot{M}_w, -6v_{w,8}$	$d_w \cos i$ (pc)	$v_0 n_{0,3}^{1/2} (\cos i)^{-1}$ (km s $^{-1}$ )	$v'_0 n'_{0,3}{}^{1/2} (\cos i)^{-1}$ (km s $^{-1}$ )	$p_{0,-9}$
1	O9.5 IV	$\simeq 0.2$	0.096	7	...	1.7
2	O9 V	$\simeq 0.2$	0.053	13	7	5.5
3	O9.5 V	$\simeq 0.2$	0.034	20	17	13
4	O7 V	0.5–2.5	0.13	8–18	$\leq 14$	2.3–11
5	O9 III+O9.5 III	1–3	0.067	22–39	19–37	17–51
6	B0 Ib	0.5–2.5	0.038	30–62	28–61	27–133
36	O8.5 V+O9 V	1–5	0.17	9–20	$\leq 17$	2.7–13
37	O9 V	$\simeq 0.2$	0.19	3.5	...	0.43
39	B0 V	$\simeq 0.2$	0.064	11	2	3.8

Complex Project examined UCAC3 and other proper motion catalogs and concluded that the data as a whole were of insufficient quality to aid in the interpretation of the X-ray source population (Broos et al. 2011). Finally, we note that a high proper motion star is not necessary to explain the morphology of ERO 21, as feedback-driven flows from the nearby Tr 14 cluster could also sculpt the associated globule into the observed “sickle” shape.

ERO 18 was previously identified by S10 (their ERO S3). The morphology and mid-IR colors of ERO 18 suggest that it may be a wind-carved cavity in a larger molecular cloud rather than a bow shock (Figure 7). ERO 18 presents a special case for the orientation and offset distance measurements (Section 2.2); because the arc is contiguous with a larger nebular structure we bisected the visible arc in lieu of using the position of peak  $8 \mu\text{m}$  emission. As with ERO 21, the colors of ERO 18 are consistent with PAH-dominated emission (Figure 6). Our 2dF/AAOmega spectra give a B8 type for the star apparently associated with ERO 18, but this may be a chance alignment. A late B-star is unlikely to provide sufficient wind momentum to form a detectable ionized shock front, particularly one with such a large standoff distance as ERO 18. The driving star also has proper motion

reported in the UCAC4 catalog equivalent to  $\sim 30 \text{ km s}^{-1}$  at position angle  $65^\circ$  W of N (Zacharias et al. 2013). This proper motion is not significant given the reported errors, and in any case points in the *opposite* direction of the orientation of ERO 18 (Table 1 and Figure 7). For these reasons we do not classify ERO 18 and the apparently associated late B star as an MBS.

## 5 SUMMARY

We have identified 39 EROs in the Carina Nebula through visual inspection of *Spitzer* mid-IR images. Among these EROs are 17 candidate IR bow shocks associated with OB stars, 6 appearing as  $8.0 \mu\text{m}$  arcs, 3 as  $24 \mu\text{m}$  arcs, and the remaining 8 identified using their mid-IR colors. Six of these bow shock candidates were previously identified by S10, while the IR colors and morphologies of the remaining 3 EROs cataloged by S10 (their S1, S3, and S9—the “compact nebula” reported by Ascenso et al. 2007) favor PAH-dominated nebular structures over bow shocks.

The majority of bow shock candidates (10) are oriented inward toward the central ionizing clusters of the

Carina Nebula (Figure 3). These are examples of *in situ* bow shocks where the winds of late O/early B stars interact with ambient ISM flows driven by the global expansion of the H II region, as observed in M17 and RCW 49 by P08. Five bow shock candidates have transverse or outward orientations that could indicate high space velocities consistent with runaway OB stars, as previously observed in NGC 6611 (Gvaramadze & Bomans 2008), Cygnus-X (Kobulnicky et al. 2010), and NGC 6357 (Gvaramadze et al. 2011), or locally non-radial flows of plasma photoevaporating off of nearby molecular cloud surfaces. Analysis of measured standoff distances demonstrates that the ambient momentum flux in the expanding Carina H II region is comparable to the M17 and RCW 49 H II regions (P08).

We find that all 8.0  $\mu\text{m}$  bow shock candidates occupy a box-shaped region on the [4.5] – [5.8] vs. [5.8] – [8.0] color plane that is largely free of nebular PAH knots, YSOs, and PAH-dominated external galaxies (Figure 5). We further find that all candidate bow shocks have [8.0] – [24] > 2 mag, providing an additional means of separating them from PAH knots (Figure 6). Because the mid-IR extinction law is observed to be approximately flat from the [4.5] through [24] *Spitzer* filters (Flaherty et al. 2007), these color cuts are conveniently reddening-free. These cuts provide a simple prescription for identifying candidate unresolved bow shocks based on MIR colors. It is possible, for example, that some of the reddest sources classified as YSOs in the MIREs catalog (Povich et al. 2013) are actually unresolved bow shocks.

## ACKNOWLEDGEMENTS

We thank the anonymous referee for their positive and useful suggestions to help improve this work. We thank S. R. Majewski and R. Indebetouw for providing early access to advanced data products from the Vela–Carina survey and M. V. McSwain for reducing the 2dF/AAOmega spectroscopic data and performing the spectral classifications for OB stars associated with EROs. We gratefully acknowledge support from NSF award AST-0847170 (CAMPARE; ALR, PI). NS received partial support from NASA through awards issued by JPL/Caltech as part of GO programs 3420, 20452, and 30848. This work is based on observations from the *Spitzer Space Telescope* GO programs 30848 (MIPSCAR; N. Smith, PI) and 40791 (VelaCarina; S. R. Majewski, PI). *Spitzer* is operated by the Jet Propulsion Laboratory, California Institute of Technology through a contract from NASA.

## REFERENCES

Allen, D. A., & Hillier, D. J. 1993, Proceedings of the Astronomical Society of Australia, 10, 338  
 Ascenso, J., Alves, J., Vicente, S., & Lago, M. T. V. T. 2007, A& A, 476, 199  
 Benjamin, R. A., Churchwell, E., Babler, B. L., et al. 2003, PASP, 115, 953  
 Brooks, K. J., Cox, P., Schneider, N., et al. 2003, A& A, 412, 751  
 Broos, P. S., Townsley, L. K., Feigelson, E. D., et al. 2011, ApJS, 194, 2

Castor, J. I., Abbott, D. C., & Klein, R. I. 1975, ApJ, 195, 157  
 Crowther, P. A., & Willis, A. J. 1993, Space Sci. Rev., 66, 85  
 Churchwell, E., Babler, B. L., Meade, M. R., et al. 2009, PASP, 121, 213  
 Everett, J., & Churchwell, E. 2010, Astronomical Society of the Pacific Conference Series, 438, 69  
 Fazio, G. G., Hora, J. L., Allen, L. E., et al. 2004, ApJS, 154, 10  
 Feigelson, E. D., Getman, K. V., Townsley, L. K., et al. 2011, ApJS, 194, 9  
 Flaherty, K. M., Pipher, J. L., Megeath, S. T., et al. 2007, ApJ, 663, 1069  
 Fullerton, A. W., Massa, D. L., & Prinja, R. K. 2006, ApJ, 637, 1025  
 Gagné, M., Fehon, G., Savoy, M. R., et al. 2011, ApJS, 194, 5  
 Gvaramadze, V. V., & Bomans, D. J. 2008, A& A, 490, 1071  
 Gvaramadze, V. V., Kniazev, A. Y., Kroupa, P., & Oh, S. 2011, A& A, 535, A29  
 Gvaramadze, V. V., Langer, N., & Mackey, J. 2012, MNRAS, 427, L50  
 Houk, N., & Cowley, A. P. 1975, University of Michigan Catalogue of two-dimensional spectral types for the HD stars. Volume I. Declinations  $-90^\circ$  to  $-53^\circ$ , Ann Arbor, MI (USA)  
 Kobulnicky, H. A., Gilbert, I. J., & Kiminki, D. C. 2010, ApJ, 710, 549  
 Majewski, S., Babler, B., Churchwell, E., et al. 2007, Spitzer Proposal, 40791  
 Muijres, L., Vink, J. S., de Koter, A., et al. 2012, A& A, 546, A42  
 Muijres, L. E., Vink, J. S., de Koter, A., Müller, P. E., & Langer, N. 2012, A& A, 537, A37  
 Ngoumou, J., Preibisch, T., Ratzka, T., & Burkert, A. 2013, ApJ, 769, 139  
 Peeters, E., Mattioda, A. L., Hudgins, D. M., & Allamandola, L. J. 2004, ApJ, 617, L65  
 Povich, M. S., Stone, J. M., Churchwell, E., et al. 2007, ApJ, 660, 346  
 Povich, M. S., Benjamin, R. A., Whitney, B. A., et al. 2008, ApJ, 689, 242 (P08)  
 Povich, M. S., Townsley, L. K., Broos, P. S., et al. 2011a, ApJS, 194, 6  
 Povich, M. S., Townsley, L. K., Broos, P. S., et al. 2011b, ApJS, 194, 14  
 Povich, M. S., Kuhn, M. A., Getman, K. V., et al. 2013, ApJS, 209, 31  
 Reed, B. C. 2003, AJ, 125, 2531  
 Rieke, G. H., Young, E. T., Engelbracht, C. W., et al. 2004, ApJS, 154, 25  
 Smith, N., Egan, M. P., Carey, S., et al. 2000, ApJ, 532, L145  
 Smith, N. 2002, MNRAS, 337, 1252  
 Smith, N. 2006a, ApJ, 644, 1151  
 Smith, N. 2006b, MNRAS, 368, 1983  
 Smith, N., & Brooks, K. J. 2007, MNRAS, 379, 1279  
 Smith, N., Ganeshalingam, M., Chornock, R., et al. 2009, ApJ, 697, L49  
 Smith, N., Povich, M. S., Whitney, B. A., et al. 2010, MN-

- RAS, 406, 952 (S10)
- Sota, A., Maíz Apellániz, J., Morrell, N. I., et al. 2014, ApJS, 211, 10
- Stetson, P. B. 1987, PASP, 99, 191
- Usov, V. V. 1991, MNRAS, 252, 49
- van Buren, D., & McCray, R. 1988, ApJ, 329, L93
- van Buren, D., Mac Low, M.-M., Wood, D. O. S., & Churchwell, E. 1990, ApJ, 353, 570
- Vink, J. S., de Koter, A., & Lamers, H. J. G. L. M. 2001, A&A, 369, 574
- Walborn, N. R., & Fitzpatrick, E. L., 1990, PASP, 102, 379
- Walborn, N. R., Howarth, I. D., Lennon, D. J., et al. 2002, AJ, 123, 2754
- Wang, J., Feigelson, E. D., Townsley, L. K., et al. 2011, ApJS, 194, 11
- Williams, P. M., van der Hucht, K. A., Sandell, G., & The, P. S. 1990, MNRAS, 244, 101
- Zacharias, N., Finch, C. T., Girard, T. M., et al. 2013, AJ, 145, 44

**Table 3.** Total IRAC and MIPS mid-IR flux densities for EROs and probable driving stars (Jy). Reported IRAC and MIPS flux densities  $F$  are background-subtracted. Irregularly shaped apertures were used to measure fluxes were drawn by hand to outline the ERO emission visible in the 8.0  $\mu\text{m}$  residual images. The 8.0  $\mu\text{m}$  source apertures were used to measure fluxes at all other bandpasses. Separate circular apertures were used to determine the median background, then the background flux density  $B$  was computed for the corresponding source aperture. EROs 36-39 are 24.0  $\mu\text{m}$  objects, for which source apertures were drawn using the 24.0  $\mu\text{m}$  emission. EROs 2, 21, and 22 do not have 24.0  $\mu\text{m}$  data because they fall in saturated regions of the MIPS mosaic.

ERO	IRAC										MIPS				
	$F_{[3.6]}$	$\delta_{[3.6]}$	$F_{[3.6]}/B_{[3.6]}$	$F_{[4.5]}$	$\delta_{[4.5]}$	$F_{[4.5]}/B_{[4.5]}$	$F_{[5.8]}$	$\delta_{[5.8]}$	$F_{[5.8]}/B_{[5.8]}$	$F_{[8.0]}$	$\delta_{[8.0]}$	$F_{[8.0]}/B_{[8.0]}$	$F_{[24.0]}$	$\delta_{[24.0]}$	$F_{[24.0]}/B_{[24.0]}$
1	11.4	0.2	2310	7.2	0.2	1804	5.3	0.1	412	12.3	0.2	2486	61.1	0.4	190
2	9.9	0.2	372	9.9	0.2	303	32.4	0.1	219	298	1	11195			
3	12.7	0.3	1287	9.6	0.2	796	14.2	0.1	562	75.1	0.5	7598	348	1	365
4	84.4	0.9	3187	63.6	0.7	2577	98.2	0.4	1125	363	1	13726	707	2	937
5	16.3	0.2	1589	10.6	0.1	1264	6.9	0.1	144	20.8	0.2	2033	32.3	0.2	55
6	16.6	0.4	1678	11.5	0.3	1361	11.3	0.2	341	53.0	0.6	5359	205	1	2173
7	1.2	0.1	280	1.0	0.1	236	5.14	0.06	422	13.3	0.2	3159	3.0	0.2	37
8	2.2	0.1	533	1.9	0.1	475	1.47	0.03	87	11.4	0.1	2715	80.3	0.2	748
9	1.9	0.1	372	2.08	0.05	549	2.41	0.03	78	3.3	0.1	626	0.2	0.1	11
10	1.4	0.1	216	1.11	0.04	180	7.7	0.1	236	21.5	0.2	3214	3.1	0.1	32
11	0.53	0.03	105	0.55	0.03	157	3.57	0.04	135	8.2	0.1	1616	3.4	0.1	137
12	0.62	0.05	198	0.39	0.03	157	2.25	0.04	174	5.7	0.1	1808	0.7	0.2	30
13	4.9	0.1	1839	3.30	0.07	1561	2.80	0.04	270	5.0	0.1	1854	12.0	0.1	194
14	1.5	0.1	213	4.8	0.1	692	18.2	0.1	527	32.0	0.2	4487	18.9	0.2	72
15	22.0	0.4	1923	14.8	0.3	1185	12.9	0.1	325	23.5	0.3	2053	66.5	0.5	122
16	0.57	0.03	94	0.53	0.03	132	2.10	0.03	61	5.6	0.1	916	1.1	0.1	36
17	3.6	0.1	935	2.60	0.07	644	2.45	0.04	218	6.6	0.1	1704	25.9	0.2	132
18	16.3	0.5	1196	9.4	0.4	925	30.3	0.4	742	70.5	1.1	5162	15	2	39
19	1.7	0.1	258	1.3	0.1	265	10.7	0.1	288	29.0	0.2	4301	4.3	0.2	127
20	16.4	0.3	1331	11.2	0.2	799	11.6	0.1	266	33.4	0.3	2707	338	1	418
21	26.9	0.3	672	19.8	0.2	476	14.68	0.3	705	422	1	10556			
22	0.92	0.03	104	0.79	0.03	83	1.58	0.02	33	13.5	0.1	1534	172	1	250
23	17.3	0.4	820	12.3	0.3	619	11.1	0.1	109	33.5	0.4	1587	59.9	0.2	239
24	3.0	0.1	295	3.2	0.1	263	8.0	0.1	292	20.6	0.2	2050	29.9	0.2	108
25	4.4	0.1	524	3.50	0.08	378	3.91	0.04	133	12.9	0.1	1546	81.6	0.3	801
26	7.6	0.2	1308	6.5	0.1	1200	8.7	0.1	317	27.1	0.2	4696	4.1	0.2	149
27	1.0	0.1	144	0.80	0.04	159	7.1	0.1	235	19.7	0.2	2968	11.3	0.1	52
28	1.8	0.1	255	1.87	0.05	271	2.35	0.03	58	6.6	0.1	929	875	1	8125
29	30.6	0.4	1765	27.3	0.3	1727	36.5	0.2	506	134.2	0.6	7739	47.9	0.2	230
30	6.2	0.1	990	6.2	0.1	961	19.1	0.1	662	43.8	0.2	7004	284	0.7	295
31	13.9	0.3	882	9.4	0.2	472	9.2	0.1	198	50.5	0.4	3194	10.2	0.1	205
32	1.5	0.1	144	1.4	0.1	207	14.9	0.1	242	43.4	0.2	4222	114.1	0.3	1123
33	4.7	0.1	618	4.5	0.1	636	8.1	0.1	230	26.8	0.2	3521	89.7	0.3	1290
34	4.8	0.1	532	4.4	0.1	642	20.0	0.1	446	55.1	0.3	6146	145	1	2379
35	16.0	0.4	1986	13.6	0.3	2434	100.0	0.4	3308	271	1	33553	3152	7	2864
36	170	2	3115	111.6	1.7	2272	118.3	1.1	519	388	3	7085	1705	12	4027
37	792	6	18910	683.9	5.0	21219	564	3	4330	463	6	11044	105	1	599
38	11.2	0.3	424	8.1	0.2	419	7.1	0.1	44	18.0	0.4	680	347	7	1370
39	147	2	4701	100.5	1.7	4173	104	1	765	161	3	5123			